

Matching seismic masses for RR Lyrae-type and oscillating red horizontal-branch stars in M4

László Molnár^{1,2}, Henryka Netzel³, Madeline Howell^{4,5}, Csilla Kalup^{1,2}, and Meridith Joyce^{1,6}

¹ Konkoly Observatory, HUN-REN Research Centre for Astronomy and Earth Sciences, MTA Centre of Excellence, Konkoly-Thege Miklós út 15-17, H-1121, Budapest, Hungary

e-mail: molnar.laszlo@csfk.org; lmolnar@konkoly.hu

² ELTE Eötvös Loránd University, Institute of Physics and Astronomy, 1117, Pázmány Péter sétány 1/A, Budapest, Hungary

³ Institute of Physics, École Polytechnique Fédérale de Lausanne (EPFL), Observatoire de Sauverny, 1290 Versoix, Switzerland

⁴ School of Physics and Astronomy, Monash University, Clayton, VIC 3800, Australia

⁵ ARC Centre of Excellence for Astrophysics in Three Dimensions (ASTRO-3D), Australia

⁶ University of Wyoming, 1000 E University Ave, Laramie, WY USA

ABSTRACT

Globular clusters offer a powerful way to test the properties of stellar populations and the late stages of low-mass stellar evolution. In this paper we study oscillating giant stars and overtone RR Lyrae-type pulsators in the nearest globular cluster, M4, with the help of high-precision, continuous light curves collected by the *Kepler* space telescope in the K2 mission. We determine the frequency composition of five RRc stars and model their physical parameters with a grid of linear pulsation models. We are able, for the first time, to compare seismic masses of RR Lyrae stars directly to the masses of the very similar red horizontal branch stars in the same stellar population, independently determined from asteroseismic scaling relations. We find a close match, with an average seismic mass of $0.651 \pm 0.028 M_{\odot}$ for RR Lyrae stars and $0.657 \pm 0.034 M_{\odot}$ for red horizontal-branch stars. While the validity of our RR Lyrae masses still relies on the similarity of neighboring horizontal branch subgroups, this result strongly indicates that RRc stars may indeed exhibit high-degree, $l = 8$ and 9 non-radial modes, and modeling these modes can provide realistic mass estimates. We also determine the He content of the cluster to be $Y = 0.266 \pm 0.008$, and compare the seismic masses for our sample of RR Lyrae to theoretical mass relations and highlight the limitations of these relations.

Key words. globular star clusters – asteroseismology – RR Lyrae variable stars

1. Introduction

Masses of RR Lyrae stars are notoriously difficult to determine. This is a problem, because the masses of Horizontal Branch (HB) stars, and in particular the masses of RR Lyrae stars, located at the intersection of the HB and the instability strip of classical pulsating stars, are crucial pieces of information for stellar evolution theories and models (Catelan 2009). Masses would provide information not only on the mass distribution along the HB, but also on the amount of mass loss during the red giant phase of stellar evolution and on the accuracy of mass estimates based on pulsational envelope models, as well. Thus, many avenues of research have been already explored to determine the masses of RR Lyrae stars.

Binarity, for example, would be a straightforward way to infer dynamical masses. However, not only do we not know any eclipsing binaries with an RR Lyrae member, it is very difficult to find systems that contain an RR Lyrae star at all (Wade et al. 1999; Kennedy et al. 2014; Hajdu et al. 2015). Since *bona fide* RR Lyrae stars are considered to be very old, their companions have either evolved into white dwarfs or other stellar remnants already, or must be smaller stars, most likely still evolving along the lower main sequence as K–M dwarfs. As such, the contribution of RR Lyr companions to the total light output of the system is expected to be minimal, precluding the detection via spectral energy distributions or as double-lined spectroscopic binaries.

The dearth of eclipsing RR Lyrae stars can also be explained by the evolutionary pathways of these pulsators. These stars moved past the red giant phase without any significant interactions with a companion that could have directed the primary away from evolving onto the HB and towards binary evolution scenarios. Companions thus must be distant to avoid any mass transfer, and a distant companion orbiting a now shrunken horizontal-branch star would make the probability of observing eclipses from the system very low. The only eclipsing binary candidate system turned out to be an impostor, a Binary Evolution Pulsator (Pietrzyński et al. 2012; Karczmarek et al. 2017). In this case, mass transfer directed a much lighter primary to rapidly cross the instability strip and to experience RR Lyrae-like pulsations. We note that binarity and a limited amount of mass transfer has been proposed to explain metal-rich RR Lyrae stars, but those systems are expected to have wide orbits, too (Bohrick et al. 2024).

More indirect methods have shown increased promise, but all have their own caveats. For example, radial velocity searches are hindered by the expected long orbital periods and small signals relative to the much larger pulsation velocities. A recent work proposed new binary candidates, but it also failed to confirm the expected periastron passage of the oldest binary candidate, TU UMa (Wade et al. 1999; Barnes et al. 2021).

An alternative way to detect binaries and estimate masses is the light-time effect, but this method has been impeded by the

prevalence of the Tseraskaya–Blazhko effect¹, the quasi-periodic modulation of the pulsation amplitude and phase (Blazhko 1907; Shapley 1916; Kurtz 2022). Nevertheless, several binary candidates have been identified in the OGLE survey (Hajdu et al. 2015, 2021). And while Hajdu et al. (2021) did not address the masses of the primaries directly, these authors found a trimodal distribution in the mass functions of the secondaries.

As we have shown, dynamical methods to determine masses of RR Lyrae stars suffer from various theoretical and/or practical shortcomings. This limits us to other, more indirect, model-dependent methods. Fundamental physical parameters such as luminosity, T_{eff} and $\log g$, along with elemental abundances, can be fitted with evolutionary tracks and atmosphere models. A relation to calculate masses from other physical parameters (period, luminosity, T_{eff}) was first proposed by van Albada & Baker (1971) and by multiple authors since. However, they come with strong uncertainties in various model parameters that are very loosely constrained by observations, if at all. These include the He content of the models, the approximations chosen for internal processes like convection and overshoot, or various aspects of mass loss along the evolutionary pathway (see, e.g., Marconi et al. 2018; Anders & Pedersen 2023; Joyce & Tayar 2023; Joyce et al. 2024). Nemeč et al. (2011) used such relations to calculate masses for the RR Lyrae stars in the *Kepler* field, for example, but without providing uncertainties for them.

One way to limit uncertainties in stellar parameters is to study RR Lyrae stars in globular clusters. There are currently close to three thousand RR Lyrae stars known in 115 Galactic globular clusters (Cruz Reyes et al. 2024). For these stars, parameters like distance and metallicity can be determined accurately for the members, and using that information, the van Albada & Baker (1971) relation was employed in many cases to estimate masses. M3, for example, was studied by multiple authors, and Valcarce & Catelan (2008) determined the mass distribution for the entire HB of the cluster based on evolutionary models, and found the distribution to be potentially bimodal. However, they discuss how that finding can be complicated by limitations present in the stellar tracks. A different approach was taken by Kumar et al. (2024), who fitted the light curves of the M3 RR Lyrae variables directly, based on a grid of non-linear pulsation models. Direct light curve fitting is a promising technique (see also, Bellinger et al. 2020, and Das et al., in prep), but current one-dimensional non-linear pulsation models still cannot reproduce light curves very accurately, due to limitations in handling convection, for example (Kovács et al. 2023).

Uncertainties in evolutionary and non-linear pulsation models can also be mitigated if we turn towards asteroseismology, and model the frequencies of the oscillatory modes observed in the star (see, e.g., Kjeldsen & Bedding 1995; Aerts 2021). Incorporating asteroseismic constraints has shown great potential recently for stars outside the instability strip. However, classical pulsators like RR Lyrae stars face obstacles in this aspect, too: in these stars, most often only a single mode can be observed, severely limiting our ability to constrain physical parameters from frequencies alone. Masses for a few double-mode RR Lyrae stars have been calculated from non-linear non-adiabatic hydrodynamical simulations, (Molnár et al. 2015b), but, as mentioned before, the accuracy of non-linear models have been called into question (Smolec & Moskalik 2008).

More recently, a new method based on the discovery of low-amplitude signals in overtone RR Lyrae stars has been proposed

(Netzel et al. 2015b,c). Theoretical predictions by Dziembowski (2016) suggested that these modes may be high-order, $\ell = 8, 9$ non-radial modes, which can be calculated from linear pulsation models. Unlike modeling radial modes in the non-linear regime, fitting radial and non-radial modes together using a linear model grid is a technique very similar to the asteroseismology of red giant stars. This method was developed by Netzel & Smolec (2022), and was further explored, incorporating other observables such as T_{eff} , L and $[\text{Fe}/\text{H}]$ information into the fit in Netzel et al. (2023).

But, as we have shown, we still lack a way to test the validity of these new RR Lyrae masses through direct methods. We therefore searched for alternatives. RR Lyrae stars make up only a small portion of the He-core-burning regime, and stars exist blue- and redward of them on the HB. Indeed, the evolution of HB stars and their positions on the HB are largely defined by the mass of their H-rich envelopes, as well as the mass loss they experience before reaching the HB. At temperatures below the red edge of the instability strip, we find the red horizontal branch (rHB) stars. These stars are very similar to the RR Lyrae pulsators, except for hosting a slightly more extended envelope. Since their envelopes are also convective, these stars show solar-like oscillations instead of pulsations, and these solar-like oscillations can be analysed in a way very similar to that of red giant and red clump stars (Matteuzzi et al. 2023). If rHB and RR Lyrae stars can be observed and modeled within the same population of stars, such as in globular clusters, they can potentially offer a way to compare asteroseismic masses determined by independent methods.

This opportunity came with the *Kepler* space telescope. *Kepler* observed multiple globular clusters during the K2 mission, including the cluster closest to the Sun, Messier 4 (M4). This cluster was bright enough that seismic data was obtainable not only for the bright red giants, but fainter stars, such as the rHB stars in it, as well. Howell et al. (2022) calculated seismic masses for several stars and compared the averages of various evolutionary phases to estimate the integrated mass loss between stages in the cluster. M4 also contains several RR Lyrae stars, including overtone ones that have been observed by *Kepler*. If non-radial modes can be detected in the overtone stars, their seismic masses could be compared directly to the seismic masses of rHB stars, validating the results.

In Section 2, we process the *Kepler* data of five RRc stars observed in M4 and determine their physical parameters. In Section 3, we analyse the photometry and the frequency content of the RRc stars and fit them with seismic models. In Section 4, we compare the RRc physical parameters to the (updated) parameters of the red giant stars of the cluster, as well as to theoretical mass relations. Finally, we summarize our findings in Section 5.

2. Data and methods

The *Kepler* space telescope observed M4 during Campaign 2 of the K2 mission in late 2014 for 80 days nearly continuously. The cluster was at the edge of module 12 of the detector; hence M4 was only partially covered by the campaign.

2.1. K2 photometry

A large portion of the cluster was covered with an extended custom pixel aperture. We identified three RRc stars within this aperture: M4 V6, V42 and V61. To extract their light curves, we followed the same differential-image method based on the

¹ Ms. Tseraskaya (Ceraski) collected the data at Moscow Observatory that led to the discovery.

FITSH photometry package of Pál (2012) that we used on M80 (Molnár et al. 2023b), and on other crowded, faint, and/or moving targets (see, e.g., Molnár et al. 2015a, 2018; Kalup et al. 2021). The output for these stars is flux variations relative to the subtracted master frame. We shifted the median variations to the *Gaia* DR3 G-band average brightnesses (Gaia Collaboration et al. 2021; Riello et al. 2021).

Since M4 has a large angular diameter, it extends beyond the K2 custom aperture. We located two additional RRc stars farther away from the center (V43 and V76), on the outskirts of the cluster: these were recorded with individual pixel apertures. For these two stars, we used the simple aperture photometry (SAP) light curves provided by the mission.

Raw K2 photometric data contains systematic signals due to the limited pointing capabilities experienced by the telescope during the mission. It was found in earlier works focusing on RR Lyrae stars (Plachy et al. 2019; Bódi et al. 2022; Molnár et al. 2023b) that the best method to separate the instrumental signals from the pulsations is the K2 Systematics Correction (K2SC) method developed by Aigrain et al. (2016). We applied the same corrections here to remove fast systematics. Slow trends were then removed with the algorithm developed by Bódi et al. (2022), fitting a high-order polynomial to the light curve that is optimized for best overlap of the pulsation cycles via phase dispersion minimization. The resulting light curves are shown in Fig. 1. Photometric data is available in Appendix B.

One more target, M4 V75, which was identified as a possible RRc star by Yao et al. (1988), is located within the K2 custom aperture as well. This star, however, shows no periodic variation, confirming previous non-detections by Stetson et al. (2014) and Safonova et al. (2016).

2.2. Observational constraints

A detailed asteroseismic analysis requires further constraints on the physical parameters (such as L , T_{eff} , $\log g$ or $[\text{Fe}/\text{H}]$) of the stars. Howell et al. (2022) used scaling relations for the red giants in the cluster, which relies on luminosities and effective temperatures. These quantities can be calculated from photometry, but they require accurate corrections for interstellar extinction. Here we used the reddening map and $E(B-V)$ zero point determined specifically for M4 by Hendricks et al. (2012).

In contrast, our approach for the RRc stars is akin to peak-bagging, where we collect and fit individual oscillation peaks (Appourchaux 2003). However, since we are limited to very few modes, it is still important to constrain our modeling space with classical observables such as allowed luminosity, T_{eff} and metallicity ranges.

We collected the average brightness values of the RRc stars both in *Gaia* DR3 passbands, and in Johnson passbands from the observations of Stetson et al. (2014)². The Johnson data set is displayed in Fig. 2, with the RRc stars and the stars studied by Howell et al. (2022) highlighted. However, since input parameters for previous RRc model fits were based on *Gaia* brightnesses, we decided to use those here, as well.

First, we calculated the interstellar extinction in the *Gaia* passbands with the *seismolab* software package, which uses the *mw dust* code and the Bayestar 3D dust map for that purpose (Bódi et al. 2022; Bovy et al. 2016; Green et al. 2019). We then used the distance modulus provided by Baumgardt & Vasiliev

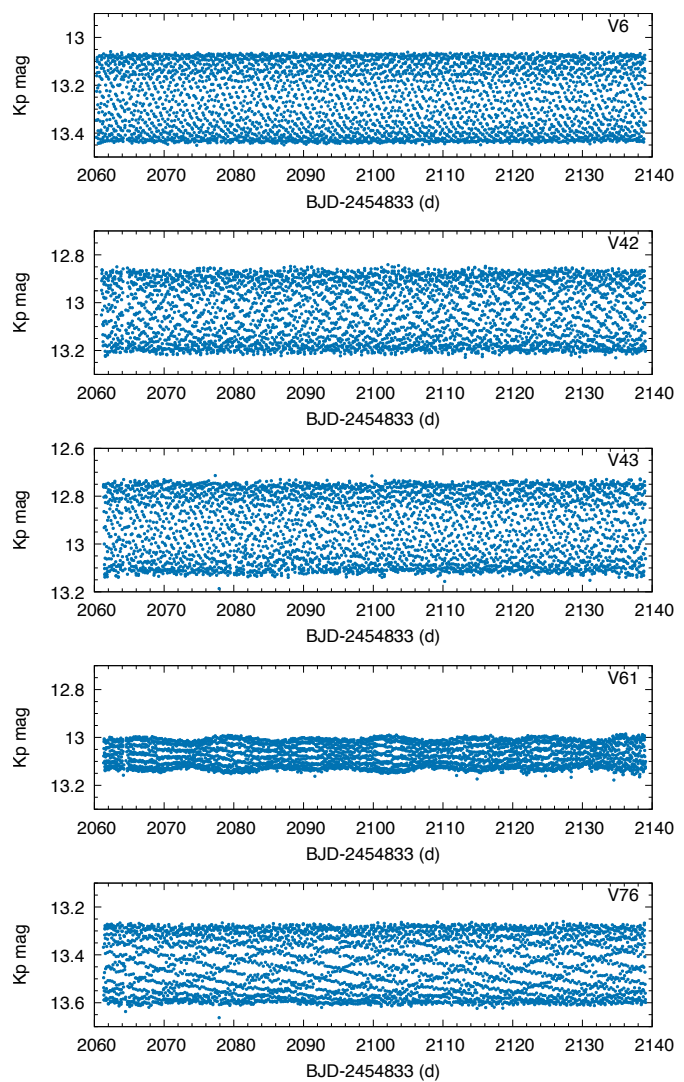


Fig. 1. Corrected K2 light curves of the five RRc stars that were targeted by the mission.

(2021), $\mu = 11.337 \pm 0.018$ mag, to convert the extinction-corrected values into absolute magnitudes.

We used M_G and $(BP - RP)_0$ to derive luminosity and effective temperature. The effective temperature T_{eff} was calculated using the relation from eq. 1 from Mucciarelli & Bellazzini (2020), which requires metallicity, $[\text{Fe}/\text{H}]$, and colour. We employed the relation derived for giant stars and colour $(BP - RP)_0$. We set the metallicity to $[\text{Fe}/\text{H}] \approx -1.1 \pm 0.07$ (Harris 1996; Marino et al. 2008; MacLean et al. 2018). The luminosity was calculated using the formula:

$$L/L_{\odot} = 10^{(-0.4(M_{\text{bol}} - M_{\text{bol}}^{\odot}))}, \quad (1)$$

where M_{bol} is a bolometric brightness of a star, and M_{bol}^{\odot} is a bolometric brightness of the Sun, set to 4.74 mag. We converted M_G to M_{bol} using bolometric correction calculated with the *Gaiadr3 Bcg* tool by Creevey et al. (2023). The input parameters to calculate bolometric correction are gravity ($\log g$), metallicity, and effective temperature. We assumed $\log g = 3$.

Metal, Z , and helium, Y , contents were calculated based on $[\text{Fe}/\text{H}]$. First, we transformed $[\text{Fe}/\text{H}]$ to $[M/\text{H}]$ using formula by Salaris et al. (1993):

² Data available at <https://www.cadc.hia.nrc.gc.ca/en/community/STETSON/homogeneous/> and at <https://www.canfar.net/storage/list/STETSON/homogeneous/>.

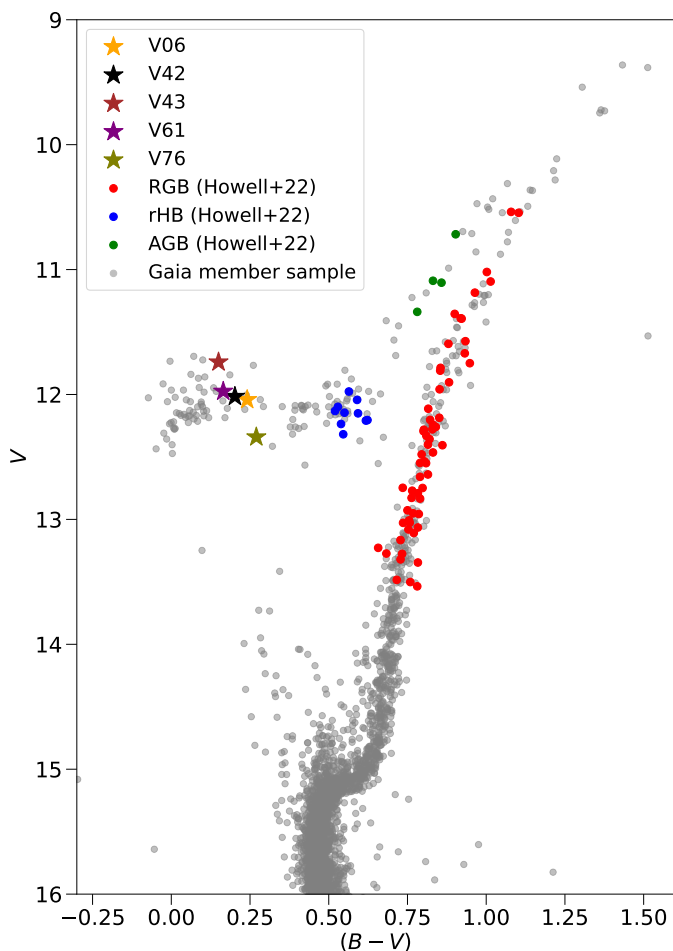


Fig. 2. Color-magnitude diagram of M4 in Johnson passbands using photometry from Momany et al. (2002) and Mochejska et al. (2002). Stars targeted by our study and by Howell et al. (2022) are highlighted with colored points. The *Gaia* membership sample is from Vasiliev & Baumgardt (2021).

$$[M/H] \approx [Fe/H] + \log(0.638 \cdot 10^{[\alpha/Fe]} + 0.362), \quad (2)$$

where $[\alpha/Fe]$ is enhancement by α elements. Then, we transformed $[M/H]$ to Z , using the relation:

$$[M/H] = \log \frac{Z}{Z_{\odot}} - \log \frac{X}{X_{\odot}}, \quad (3)$$

where Z_{\odot} and X_{\odot} are solar values, which we set to $Z_{\odot} = 0.0134$ and $X_{\odot} = 0.7381$ (Asplund et al. 2009).

Assuming that hydrogen content, X , can vary from 0.70 to 0.76, and α -element enhancement can vary from 0 to 0.4, we calculated the modeling range for Z to be 0.00086 – 0.0032.

3. Photometric results on the RRc stars

We used the *Period04* software to determine the frequency composition of each star (Lenz & Breger 2005). The detection limit was set to $S/N > 4.0$, relative to the nearby average noise level in the frequency spectrum. First, we subtracted the pulsation frequency and its harmonics, then searched for any extra signals above or below the pulsation frequency. Folded light curves and frequency spectra are displayed in Fig. 3.

3.1. Extra modes

According to Dziembowski (2016), the signals around period ratios $P/P_{01} \approx 0.63$ and 0.61 , relative to the first overtone, correspond to (the first harmonic of) $l = 8$ and $l = 9$ modes, respectively. Here we label these as f_{63} and f_{61} frequencies, although this family of modes is also called f_{61} or f_X modes collectively. The actual mode frequencies are the subharmonics of these signals at $f_{61}/2$ and $f_{63}/2$, but those are usually harder to detect due to geometric cancellation effects.

We clearly identified the modes in four stars: V6, V42, V43 and V76. We also see subtle differences between them. In V6, the subharmonic at the true pulsation frequency is the strongest, which is unusual among RRc stars as we expect the harmonic to be stronger. In V42 and V76, we detect multiple peaks and the corresponding harmonics and subharmonics. In V43, the peak appears to be incoherent and can be fitted with three close-by frequencies. Here we observe a very wide structure at the subharmonic that extends below the expected range of the f_{61} modes. However, these frequencies are not low enough to be either the fundamental mode or an f_{68} mode.

While f_{61} modes are prevalent in the RRc population of M4, we did not detect the low-frequency f_{68} mode clearly in either of the targets. The latter is a separate group of extra modes, discovered recently in RRc stars, which appear at lower frequencies ($f/f_{01} \approx 0.686$), and whose origin has not been identified yet (Netzel et al. 2015a; Benkő & Kovács 2023). The lack of detection is in agreement with the mode abundance results of Netzel et al. (2024). They found that while the f_{61} modes are most frequent around $[Fe/H] \approx -1.0$, the frequency of the f_{68} mode drops drastically above -1.3 , and the metallicity of M4 is higher than that limit.

In contrast to the results above, V61 turned out to be the rather different from the four other stars. Here we only detect significant extra frequency peaks at the subharmonic range, but not at the expected f_{61} range. The two peaks appear at period ratios 0.7335 and 0.7877. The former value may potentially correspond to the fundamental mode, with a period of 0.36168 d; however, that would put the star to $[Fe/H]$ values higher than that of M4 in the Petersen diagram (Szabó et al. 2004; Chen et al. 2023). We investigate the modulation properties of the star in Appendix A.

3.2. Petersen diagram

We present the identified f_{61} signals on a Petersen diagram in Fig. 4, showing the period ratios against the longer period (here fixed to the first overtone). We plot the M4 results in red against the points presented by Molnár et al. (2023b). We find that the points line up well with other samples that have moderate metallicities, such as the bulge and NGC 6362. In this regime most frequencies clearly fall onto the main ridges at period ratios $P_1/P_X \approx 0.632$ and 0.613 , corresponding to the $\ell = 8$ and 9 modes. We also detect signals in the middle ridge, which Dziembowski (2016) interprets as combination frequencies. Further signals appear below, at $P_1/P_X \approx 0.605$ which might also be combination peaks. We did not detect any $\ell = 10$ peaks which should be at $P_1/P_X \approx 0.6$ or below, according to Dziembowski (2016).

3.3. Comparison with other photometric results

The K2 observations were analysed before by Wallace et al. (2019a) who searched the cluster for new variables. They de-

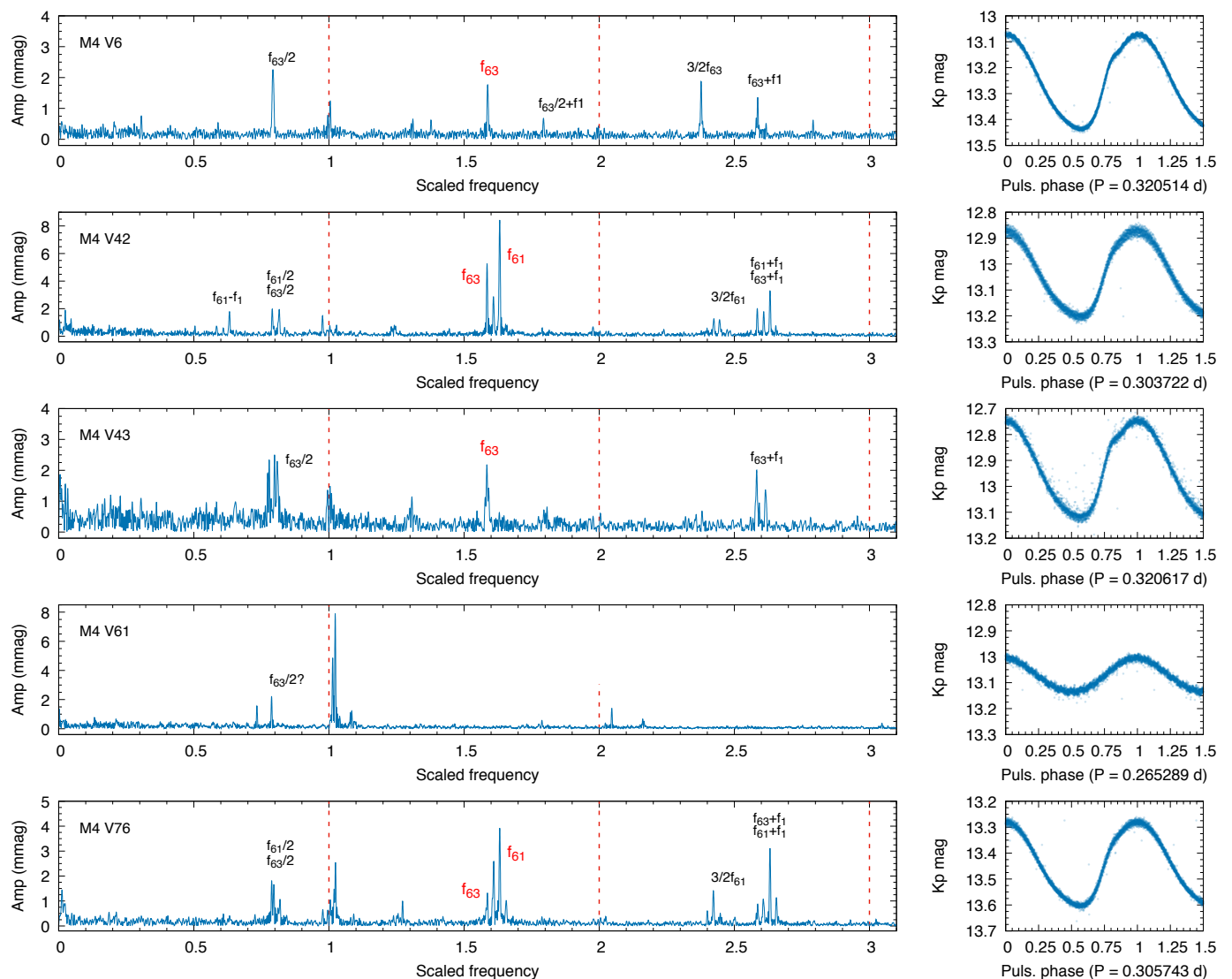


Fig. 3. Left: Fourier spectra of the five RRc stars. Here we removed the main pulsation frequency and its harmonics belonging to the first overtone to reveal the low-amplitude extra modes. Modes are labeled with red, and combination frequencies with black. Right: light curves folded with the first overtone period.

tected higher scatter in V61 than in other RR Lyrae stars, but did not recognize it as modulated. They also detected two stars they classified as millimagnitude RR Lyrae stars (Wallace et al. 2019b). Both of those two stars show only a single periodicity.

Ground-based multicolor photometry was collected for the RR Lyrae members (among others) by Stetson et al. (2014). They did not recognize V61 as a modulated star either, although upon reanalysis of their photometry, a side peak is visible. The only other star common with our targets that has a useful amount of time series photometry is V6. There a frequency signal is marginally detectable at the position of the subharmonic ($f_{63}/2$). This shows that seismic modeling of RRc stars requires extensive, high-precision photometry to detect the low-amplitude extra modes.

3.4. RRc pulsation models

For each star, we calculated pulsation models to match the observed first-overtone period and period ratio(s). To calculate the theoretical models, we used the envelope pulsation code of

Dziembowski (1977). The input physical parameters required by the code are mass, luminosity, effective temperature, hydrogen and metal abundances. Additionally, this code requires an approximate value of dimensionless frequency for the non-radial mode. We followed the approach of Netzel & Smolec (2022) for individual calculations. Namely, we used the estimates that relate non-radial mode frequencies from the linear fits to sequences in the Petersen diagram (see Equations 4 and 5 in Netzel & Smolec 2022), which were then converted to dimensionless frequencies, σ , using the formula from Eq. 6 in Netzel & Smolec (2022). Furthermore, we set the range of possible starting values of non-radial mode frequencies to $\sigma \pm 0.1$. Consequently, for each model we were able to get the non-radial mode with the highest driving rate, i.e., it is the most strongly trapped in the envelope.

In order to find the best matches between periods and period ratios in theoretical models and in observed values for each star, we employed genetic algorithms³, which used the pulsation code with different input physical parameters. The ranges of physical

³ We used a Python genetic algorithm library <https://github.com/rmsolgi/geneticalgorithm>

Table 1. Input parameter ranges, pulsation periods and period ratios for each RRc star that we used for modeling. PR1 and PR2 are the mode period ratios relative to the first overtone. Mass ranges are left deliberately wide to accommodate realistic values over the grid.

	V6	V42	V43	V61	V76
$M (M_{\odot})$	0.5 – 0.9	0.5 – 0.9	0.5 – 0.9	0.5 – 0.9	0.5 – 0.9
$\log L/L_{\odot}$	1.50 – 1.54	1.51 – 1.543	1.46 – 1.66	1.52 – 1.54	1.46 – 1.69
$\log T_{\text{eff}}$	3.79 – 3.821	3.80 – 3.83	3.80 – 3.86	3.80 – 3.84	3.80 – 3.88
X	0.7 – 0.76	0.7 – 0.76	0.7 – 0.76	0.7 – 0.76	0.7 – 0.76
Z	0.00086 – 0.0032	0.00086 – 0.0032	0.00086 – 0.0032	0.00086 – 0.0032	0.00086 – 0.0032
P_{10} (d)	0.320506	0.303719	0.320622	0.265290	0.305737
PR1	0.63005	0.63095	0.63106	0.63476	0.63076
PR2	–	0.61268	–	–	0.61327

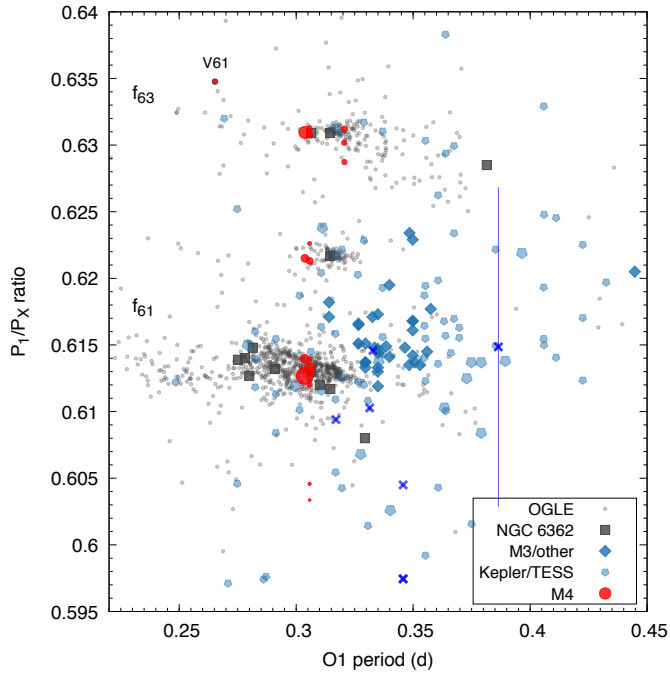


Fig. 4. Petersen diagram of the f_{61} -type modes. Here we plot signals detected in M4 (in red) over existing literature data. Frequency peaks fall onto the main ridges discovered in the OGLE data. Positions of the f_{61} and f_{63} ridges are labelled respectively.

parameters were set based on observational constraints (see Table 1). In the case of mass, we set a wide range of $0.5 - 0.9 M_{\odot}$ to accommodate any realistic mass result. For each star, we executed 100 separate runs. For each run we set the maximum number of iterations to 150, population size of 100, mutation probability of 0.1, elitist ratio to 0.01, crossover probability to 0.5, and parents portion to 0.3. We note that we performed calculations with different parameters for genetic algorithms beforehand, including the numbers of populations and iterations, to ensure that the results are robust. The values and errors of physical parameters were derived as the means and standard deviations of the results from each of the hundred individual runs.

Calculated ranges of physical parameters used to constrain the models for each star are summarized in Table 1.

4. New and revised physical parameters

With the RRc physical parameters obtained, we proceeded to compare them to parameters of other RR Lyrae stars, as well as to the average properties of M4. For further comparison, we

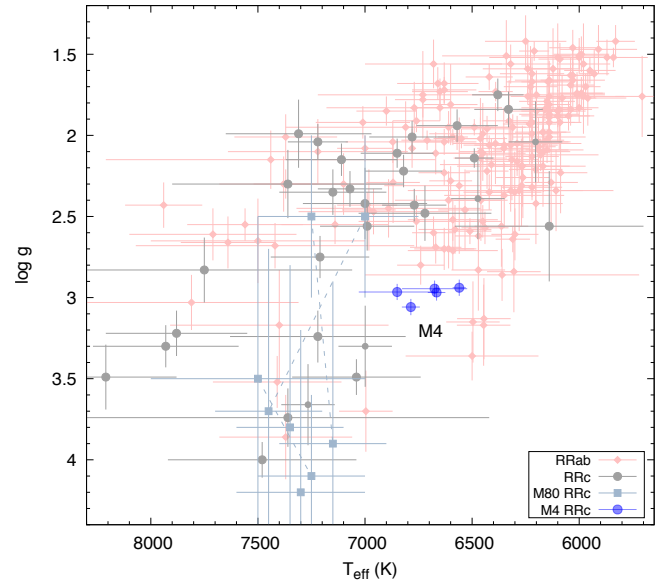


Fig. 5. Positions of the seismically determined T_{eff} and $\log g$ values for the five RRc stars in M4, against the spectroscopically observed RRc stars in the $T_{\text{eff}}-\log g$ plane, as collected by Molnár et al. (2023b).

recalculated the masses for the oscillating rHB stars originally studied in Howell et al. (2022), too.

4.1. RR Lyrae masses and other physical parameters

As listed in Table 2, the masses of four out of the five RRc stars are within $0.06 M_{\odot}$, between 0.631 and $0.683 M_{\odot}$ with an average uncertainty of $\pm 0.022 M_{\odot}$. The only outlier is the modulated star, V61, at $0.751 M_{\odot}$, but for that star our mode identification was more uncertain. However, mass outliers exist among the other evolutionary stages, such as among the rHB stars in the cluster as well. These masses align well with the mass-period distribution of RRc stars published by Netzel et al. (2023).

We compared the calculated T_{eff} and $\log g$ values to the distribution of RR Lyrae stars presented by Molnár et al. (2023b). As Fig. 5 shows, the stars belong to the cooler RRc stars, lying between $6500-7000$ K, with $\log g$ values being very close to 3.0 for all five stars. For chemical composition, we find average bulk abundances of $X = 0.734 \pm 0.0075$ and $Z = 0.0019 \pm 0.0002$. These values indicate a He abundance of $Y = 0.266 \pm 0.008$ for M4.

The comparison of the mass ratio of heavy elements, Z , to the observed $[\text{Fe}/\text{H}]$ index is not straightforward, as it is influenced by the abundance differences of individual elements (see,

Table 2. Modeled physical parameters of the five RRc stars based on seismic modeling.

	V06	V42	V43	V61	V76
$M (M_{\odot})$	0.631 ± 0.016	0.647 ± 0.014	0.683 ± 0.035	0.751 ± 0.021	0.667 ± 0.026
$\log L (L_{\odot})$	1.519 ± 0.011	1.529 ± 0.010	1.578 ± 0.054	1.536 ± 0.009	1.593 ± 0.046
T_{eff}	6560 ± 31	6666 ± 41	6675 ± 152	6786 ± 42	6850 ± 179
$\log g$	2.9394 ± 0.0033	2.9683 ± 0.0034	2.9452 ± 0.0044	3.0581 ± 0.0029	2.9652 ± 0.0053
X	0.736 ± 0.016	0.732 ± 0.018	0.730 ± 0.018	0.726 ± 0.016	0.745 ± 0.016
Z	0.0022 ± 0.0006	0.0015 ± 0.0004	0.0019 ± 0.0007	0.0027 ± 0.0003	0.0012 ± 0.0003

e.g., Hinkel et al. 2022). Nevertheless, we can give an estimate for the correctness of our seismic Z values. Following the relations described in Section 2.2, in reverse order, and using an α -enhancement of $[\alpha/\text{Fe}] = 0.39 \pm 0.05$ (Marino et al. 2008), we get an average seismic $[\text{Fe}/\text{H}]$ of -1.13 ± 0.05 for the five RRc stars, which agrees with the spectroscopic $[\text{Fe}/\text{H}]$ value of the cluster.

4.2. Seismic masses for red giants and the average rHB mass

Pressure modes in solar-like oscillators – such as red giants – are characterized by two global seismic parameters; the large frequency separation, $\Delta\nu$, and the frequency of the maximum acoustic power, ν_{max} . These quantities are correlated to stellar properties, which are used to derive seismic mass scaling relations (Ulrich 1986; Brown et al. 1991; Kjeldsen & Bedding 1995). For time-series photometry with short baselines (e.g. the K2 mission), it has been shown that accurate asteroseismic masses can be measured independently of a $\Delta\nu$ estimate (e.g. Howell et al. 2022, 2024). This method uses the following scaling relation:

$$\left(\frac{M}{M_{\odot}}\right) \approx \left(\frac{\nu_{\text{max}}}{\nu_{\text{max},\odot}}\right) \left(\frac{L}{L_{\odot}}\right) \left(\frac{T_{\text{eff}}}{T_{\text{eff},\odot}}\right)^{-7/2}. \quad (4)$$

We use the red giant sample and their corresponding K2 light curves from Howell et al. (2022) to measure seismic masses using this relation above. They detected solar-like oscillations in 75 red giants across three phases of evolution (RGB, rHB and early AGB), and used the pySYD pipeline (Chontos et al. 2022) to measure the asteroseismic parameters. We adopt the Howell et al. (2022) estimates for T_{eff} and luminosity, although not their ν_{max} determinations. Here we report updated measurements of ν_{max} and the corresponding uncertainty for each star using a new asteroseismic pipeline, pyMON (Howell et al., in prep).

The pyMON pipeline is an adaptation of pySYD (see Chontos et al. 2022 for more details), where the main difference is that $\Delta\nu$ is not measured. In both pipelines, the power spectrum is smoothed using an estimate for $\Delta\nu$. pyMON substitutes this measurement with an estimate from a calibrated $\Delta\nu$ - ν_{max} scaling relation (Stello et al. 2009; Howell et al. 2022). This is useful for low signal-to-noise data (e.g. our M4 photometry), because it is difficult to measure an accurate $\Delta\nu$. A comparison between the pySYD and pyMON methods shows that the measurement of ν_{max} remains consistent, however there is a reduction by a factor of ~ 2 in the ν_{max} uncertainty, due to the reduced uncertainty in $\Delta\nu$. Consequently, this results in a decrease in the seismic mass uncertainties by a factor of ~ 1.5 .

We provide our individual seismic masses in the bottom panel of Figure 6. Note that we have removed the stars identified as mass outliers in Howell et al. (2022), and also limited the RGB sample to below the luminosity bump (hereby known as

lower RGB or LRGB). This ensured there was no bias to lower masses due to any mass loss that might have occurred. In the top panel of Figure 6, we represent the distribution of our masses as kernel density estimation (KDE) functions for each evolutionary phase. A KDE is calculated by modelling each data point as a Gaussian, adopting the mass as the mean and the uncertainty as the standard deviation. The final KDE is the summation of the Gaussian components, where the area has been normalised to a value of one.

To estimate a new average mass for the HB sample, we determine the peak value of the corresponding KDE. This represents the mode mass for this sample, and was measured to be $0.655 \pm 0.007 M_{\odot}$. The uncertainty is calculated as the standard error on the mean. Our average HB mass is consistent with the value found previously in Howell et al. (2022). This was similarly found for the RGB and early AGB samples, where we calculated average masses of $0.80 \pm 0.009 M_{\odot}$ and $0.55 \pm 0.01 M_{\odot}$ respectively⁴. Individual and average masses relative to the calculated luminosities are plotted in Fig. 7.

The integrated mass loss rates between evolutionary phases are also consistent with Howell et al. (2022). The mass loss from the lower RGB to the HB decreases slightly to $\Delta M_{\text{RGB-HB}} = 0.145 \pm 0.011$, whereas we find a mass loss from $\Delta M_{\text{HB-AGB}} = 0.105 \pm 0.013$ from the HB to the early AGB.

We plot the distributions of the masses along the HRD in Fig. 8. We also include a MIST⁵ (MESA Isochrones and Stellar Tracks; Choi et al. 2016) isochrone for comparison. This isochrone has an age of 12.2 Gyr, an average of various literature sources for M4 (Cabrera-Ziri & Conroy 2022). Since MIST does not offer α -enhanced isochrones, we use a value of $[\text{Fe}/\text{H}] = -0.9$ to emulate the higher $[\alpha/\text{Fe}]$ abundances, based on the scaling described by Joyce et al. (2023). The mass loss prescriptions used by MIST for low-mass stars are $\eta_R = 0.1$ and $\eta_B = 0.2$ for the RGB and AGB phases, following the (Reimers 1975) and Bloeker (1995) schemes, respectively. Colors represent masses: it is clear that the conservative mass loss prescription used in MIST's pre-computed isochrone database does not capture the true amount of mass loss in the cluster. This is most evident in the later evolutionary stages: while the isochrone has masses around 0.82 – $0.83 M_{\odot}$ in the RGB, this only drops to 0.79 by the time of the HB and early AGB, which is significantly higher than the observed values. A consequence of the overly conservative mass loss prescription is that the isochrone barely reaches the red edge of the RHB region and therefore cannot reproduce the structure of the HB at all. We note that mass loss parameters cannot be adjusted in MIST through the web interface, either.

⁴ Note Howell et al. (2022) used the mean mass as their average mass scale. In this paper, we adopt the same method as Howell et al. (2024) of measuring the mode mass of the KDE distributions to determine the average mass, leading to small discrepancies. However, both average mass measures are consistent within uncertainties.

⁵ <https://waps.cfa.harvard.edu/MIST>

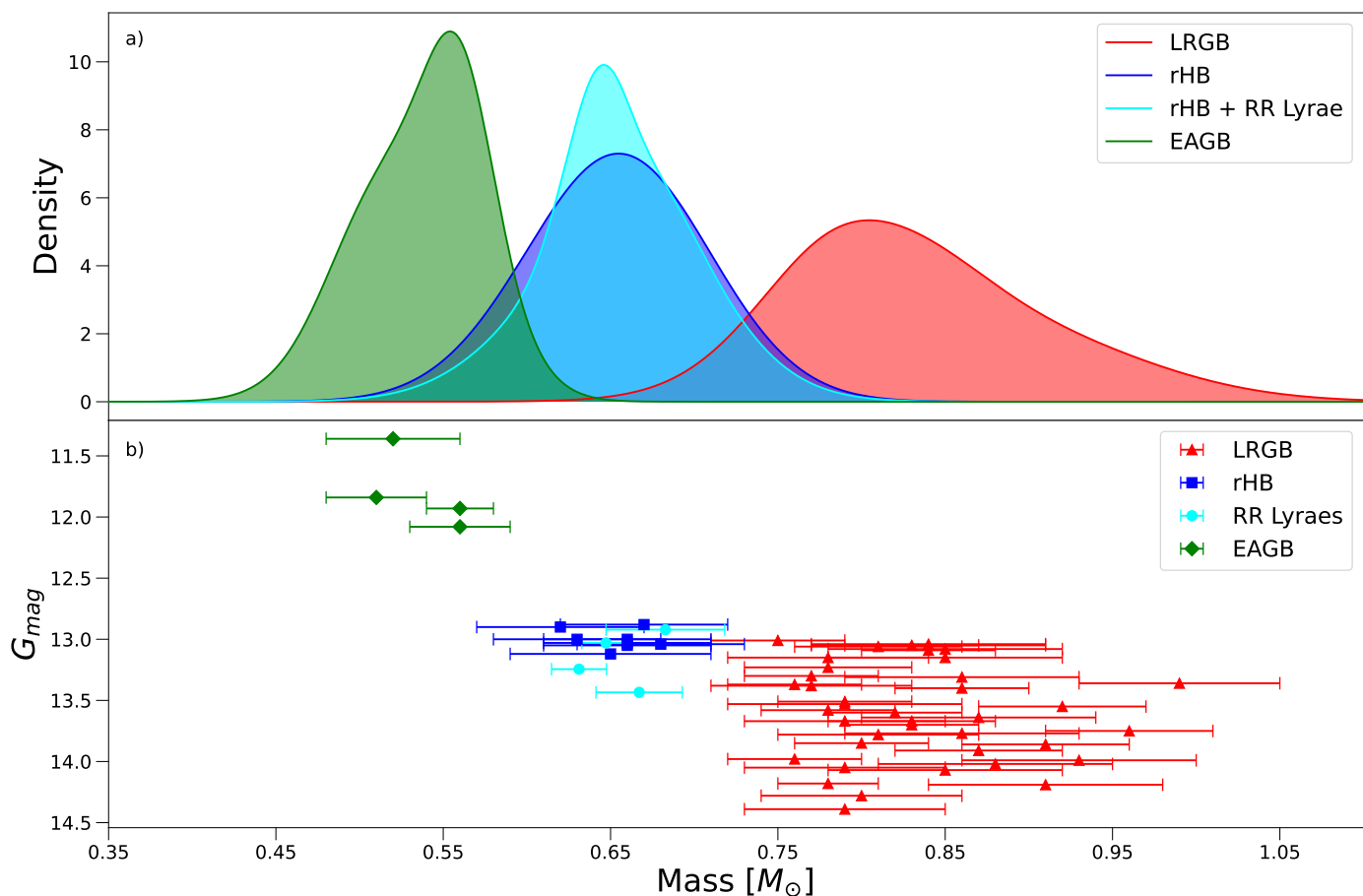


Fig. 6. a) The mass distributions (calculated as KDEs) for the M4 sample of red giants and RR Lyraes. We have separated the KDEs into evolutionary phases. For the HB sample, we have included a KDE consisting of just the rHB sample (blue), and a KDE which combines both the rHB and RR Lyrae samples (cyan). We note that the area of each KDE is normalised to one, and as such the heights of the distributions do not correspond to sample sizes. b) Individual masses for the red giant and RR Lyrae samples plotted against *Gaia* magnitude.

Table 3. Average masses of each evolutionary group.

Evolutionary stage	Average mass (M_{\odot})	Uncertainty (M_{\odot})
Lower RGB	0.800	0.009
Upper RGB	0.717	0.012
HB (all)	0.655	0.007
red HB	0.657	0.034
RRc stars	0.651	0.028
early AGB	0.550	0.010

Our results indicate that for old, low-mass stellar populations, such as globular clusters, pre-packaged MIST isochrones (and any other isochrone set with similarly conservative mass loss prescriptions) can only reliably reproduce the masses of stars up to the lower RGB, before reaching the red giant branch bump. This highlights the importance of cluster seismology and realistic mass loss estimates, because these studies can provide the first observational constraints on the required level of mass loss through the later stages of low-mass stellar evolution.

4.3. Comparison of the rHB and RRc masses

As we discussed in Section 1, estimating the masses of RR Lyrae stars in a model-independent way is an extremely difficult task. While evolutionary models can be used to constrain HB masses in globular clusters (see, e.g., Gratton et al. 2010; Howell et al.

2024; Kumar et al. 2024), and masses for RRd stars can be estimated from non-linear models (Molnár et al. 2015a), these approaches still need independent verification. Here we present, for the first time, simultaneous mass estimates based on two independent seismic approaches for stars along the HB in a globular cluster. And although these seismic models and scaling relations could still contain their own model uncertainties, they can now be verified against each other.

For M4, we found a combined HB mass of $0.655 \pm 0.007 M_{\odot}$. If we split this sample into their constituent RR Lyrae and rHB parts, we find average masses of $M_{\text{rHB}} = 0.657 \pm 0.034 M_{\odot}$ and $M_{\text{RRc}} = 0.651 \pm 0.028 M_{\odot}$, respectively. A small non-zero difference is in agreement with the evolutionary predictions that stellar (envelope) masses along the HB decrease towards the blue (Salaris & Cassisi 2006). Therefore, we can conclude that our two seismic mass estimates, the scaling relations for rHB stars, and the linear RRc model grid of Netzel & Smolec (2022), are in agreement. Thus, we may conclude that fitting the f_{61} modes offers a reliable way to estimate RR Lyrae star masses, even if it is only available for overtone stars.

4.4. Comparison with mass relations

Relations to calculate masses for RR Lyrae, or more broadly for HB stars from observational constraints, have been given by multiple authors, derived from pulsation and evolutionary

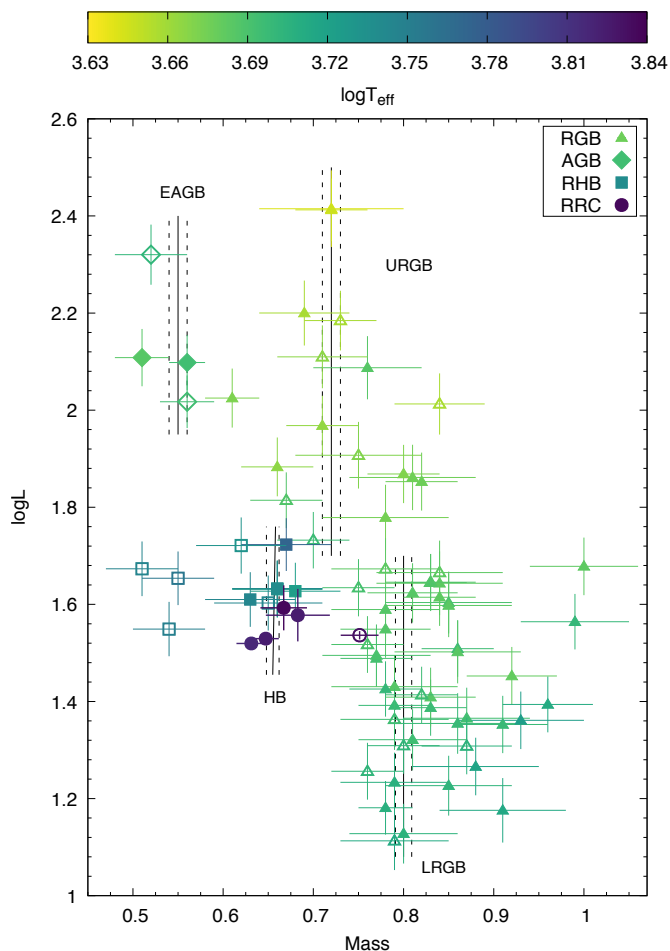


Fig. 7. The distribution of masses with increasing luminosity among the evolutionary groups. Lines indicate the average masses and uncertainties.

models. Here we compare seven prescriptions with our seismic masses. The first widely adopted relation on dependence of the pulsation period on the physical parameters (M , L , T_{eff}) was published by van Albada & Baker (1971). This was later refined and updated by multiple authors, also incorporating a metallicity term (Bono et al. 1997; Jurcsik 1998; Marconi et al. 2003; Di Criscienzo et al. 2004; Marconi et al. 2015). A more general relation between mass, color and metallicity was given for HB stars by Gratton et al. (2010).

The accuracy of these prescriptions, however, strongly depend on the modeling choices and uncertainties intrinsic to parameter choices, which are not often explored. Furthermore, many prescriptions are based on T_{eff} and L values, which have to be converted from observations and have many uncertainties and potential parameter degeneracies themselves. Converting apparent brightness to theoretical luminosity, for example, involves uncertainties in the distance of the object, in the amount of interstellar absorption between the observer and the object, and even in the calculation of the bolometric correction. Similarly, converting observed colors to T_{eff} involves uncertainties coming from interstellar absorption and the choice of extinction law parameter, as well as from the accuracy of the calibration of the color- T_{eff} conversion scales themselves.

With these limitations in mind, we calculated the RR Lyrae masses using these relations and compared them to our seismic results in two ways. First we used the classical constraints, L

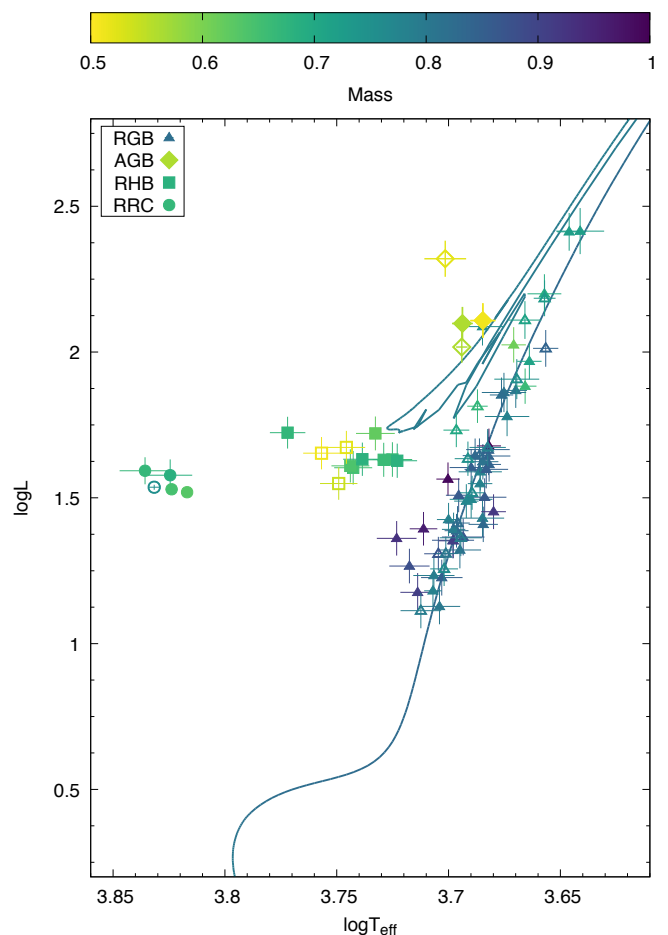


Fig. 8. The seismic HRD of M4. Here we show stars in the $\log L - T_{\text{eff}}$ plane for which masses are available. Colors indicate stellar mass. The gap in the HB between RRc and rHB stars reside, for which no mass estimate is available. The solid line is a MIST isochrone with an age of 12.2 Gyr and an $[\text{Fe}/\text{H}]$ index of -0.9 .

and T_{eff} values, computed from the *Gaia* photometry, which also served as initial values for our seismic model fits. These results are plotted in the left panel of Fig. 9. As the figure shows, the values are generally in the right range, between 0.55 and $0.8 M_{\odot}$, however, differences from the seismic values can reach $0.1 M_{\odot}$, and uncertainty ranges can be even wider than that, ranging from ± 0.03 to $\pm 0.12 M_{\odot}$.

We then recalculated the masses using the L and T_{eff} values obtained from the seismic model fits listed in Table 2, and plotted them in the right panel of Fig. 9. In contrast with the results above, these correlate very well with our seismic masses. The matches are not perfect, however, as clear systematic differences are visible. Most relations give results very similar to the original one published by van Albada & Baker (1971), underestimating the masses by an average difference of -0.020 to $-0.028 M_{\odot}$, relative to the seismic masses. The only relation that overestimates the masses is that of Marconi et al. (2015), with an average difference of $+0.032 M_{\odot}$. These results highlight the true difference between various models and their parameter choices, rather than the uncertainties coming from the observations. The main source of observational uncertainty left in these fits is in the frequencies of the modes we fit.

Gratton et al. (2010) determined a different mass relation based on the $B - V$ (or $V - I$) color indices and $[\text{Fe}/\text{H}]$ indices

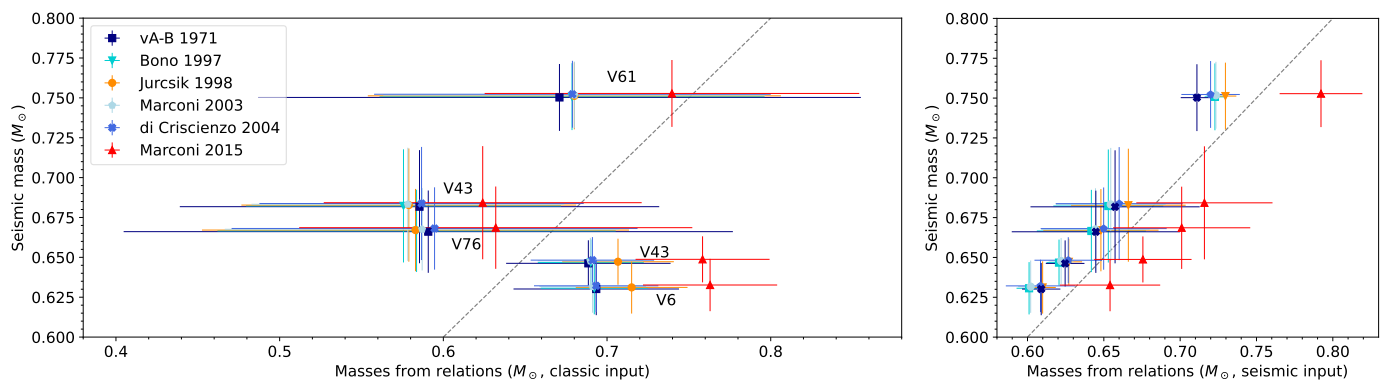


Fig. 9. Comparison of the RRc masses with results from various mass relations based on physical parameters. On the left: masses calculated from classical observational constraints obtained for L and T_{eff} . Right: masses calculated from the L and T_{eff} outputs produced by our seismic results listed in Table 2. Seismic masses are shifted by small amounts in both plots to make individual error bars visible. The dashed line is the identity line in both plots.

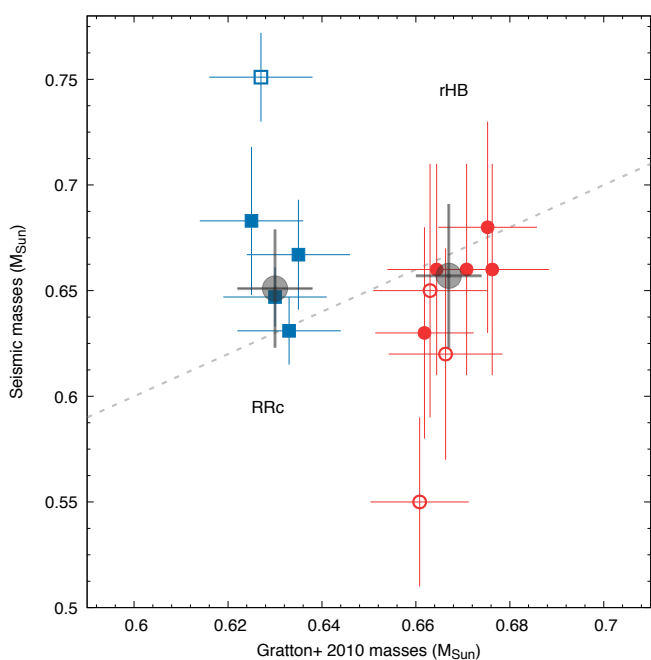


Fig. 10. Comparison of the seismic HB masses, both for the RRc and rHB stars, with the mass relation published by Gratton et al. (2010). Empty symbols indicate marginal detections. Large grey symbols indicate the averages for both groups. The dashed line is the identity line.

of HB stars. We calculated the masses of both the RRc and the rHB stars using our dereddened $B-V$ colors. The results are displayed in Fig. 10. This relation results in a larger mass difference ($0.037 M_{\odot}$) between the two groups than what we found from the seismic data. We suspect that this difference is coming from the fact that the relation is based on zero-age HB stellar models, whereas the stars in M4 are not necessarily on the ZAHB, but rather at evolutionary stages dictated by their common ages and thus common masses.

5. Conclusions

Determining the masses of RR Lyrae variables is a notoriously difficult task. While relations based on physical parameters exist, and pulsational masses can, in principle, provide masses for

double-mode stars, these are strongly model-dependent methods that could not be verified by independent mass estimates. Asteroseismology offers a new way to determine stellar masses (Aerts 2021). While seismic masses still depend on stellar envelope models and on the validity of scaling relations, they can be tested against other observational techniques, e.g., dynamical masses in eclipsing binaries.

Globular clusters, such as M4, provide an opportunity to probe the late stages of low-mass stellar evolution. Building on the unique capabilities of the *Kepler* space telescope, we calculated new, more accurate masses for the oscillating giant stars using asteroseismic scaling relations and v_{max} values determined with the new *pyMON* code (Howell et al., in prep.). We then analysed the overtone RR Lyrae stars in the cluster and determined their masses using peak-bagging and fitting the frequencies with the seismic model grid of Netzel & Smolec (2022). With these, we were able to relate RR Lyrae seismic masses to seismic masses of red HB stars, and found that they match each other closely. Furthermore, we estimate a He content of $Y = 0.266 \pm 0.008$ for the cluster from our models.

While our result is not yet a direct measurement of RR Lyrae masses, as it relies on the assumption that RR Lyrae and rHB stars in the cluster have similar masses, we were able to test model-dependent seismic (or pulsational) masses against independent mass estimates for the first time. We find that the average RRc and rHB masses agree within the errors, with the RRc stars having slightly lower masses, as expected from the structure of the HB. We compared the modeled physical parameters of the RRc stars to various relations between M , L , T_{eff} and the pulsation periods, and found that while they generally agree, systematic differences do exist. We also show, however, that the usability of these relations is rather limited, as L and T_{eff} values have to be determined very accurately, otherwise the calculated masses will be very uncertain.

This study not only tests RR Lyrae masses for the first time, but it also lends further support to the hypothesis of the f_{61} modes being high-order ℓ modes, as proposed by Dziembowski (2016). Therefore, it is now possible to estimate masses for field RRc and RRd stars as well, where enough modes can be detected from high-precision photometry (Netzel & Smolec 2022; Netzel et al. 2023). Furthermore, RRc stars now offer a way to measure masses on the HB in globular clusters, even where rHB stars are too faint for asteroseismology. RR Lyrae stars thus open up a new way to study mass loss in more clusters, either with *Kepler*, or with future instruments, such as the *Roman* Space Telescope

(Howell et al. 2024; Molnár et al. 2023a) or the HAYDN telescope project, which is designed specifically to observe dense stellar fields (Miglio et al. 2021).

Acknowledgements. This research was supported by the ‘SeismoLab’ KKP-137523 Élvirol grant of the Hungarian Research, Development and Innovation Office (NKFIH). Cs.K. was supported by the ÚNKP-23-3, New National Excellence Program of the Ministry of Culture and Innovation from the source of the National Research, Development and Innovation Fund. This research has received support from the European Research Council (ERC) under the European Union’s Horizon 2020 research and innovation programme (Grant Agreement No. 947660). H.N. is funded by the Swiss National Science Foundation (award PCEFP2_194638). M.J. gratefully acknowledges funding of MATISSE: *Measuring Ages Through Isochrones, Seismology, and Stellar Evolution*, awarded through the European Commission’s Widening Fellowship. This project has received funding from the European Union’s Horizon 2020 research and innovation programme. This research made use of NASA’s Astrophysics Data System Bibliographic Services, as well as of the SIMBAD database operated at CDS, Strasbourg, France.

References

- Aerts, C. 2021, *Reviews of Modern Physics*, 93, 015001
- Aigrain, S., Parviainen, H., & Pope, B. J. S. 2016, *MNRAS*, 459, 2408
- Anders, E. H. & Pedersen, M. G. 2023, *Galaxies*, 11, 56
- Antipin, S. V. & Jurcsik, J. 2005, *Information Bulletin on Variable Stars*, 5632, 1
- Appourchaux, T. 2003, *Ap&SS*, 284, 109
- Asplund, M., Grevesse, N., Sauval, A. J., & Scott, P. 2009, *ARA&A*, 47, 481
- Barnes, Thomas G., I., Guggenberger, E., & Kolenberg, K. 2021, *AJ*, 162, 117
- Baumgardt, H. & Vasiliev, E. 2021, *MNRAS*, 505, 5957
- Bellinger, E. P., Kanbur, S. M., Bhardwaj, A., & Marconi, M. 2020, *MNRAS*, 491, 4752
- Benkó, J. M. & Kovács, G. B. 2023, *A&A*, 680, L6
- Blažko, S. 1907, *Astronomische Nachrichten*, 175, 325
- Bloecker, T. 1995, *A&A*, 297, 727
- Bobrick, A., Iorio, G., Belokurov, V., et al. 2024, *MNRAS*, 527, 12196
- Bódi, A., Szabó, P., Plachy, E., Molnár, L., & Szabó, R. 2022, *PASP*, 134, 014503
- Bono, G., Caputo, F., Castellani, V., & Marconi, M. 1997, *A&AS*, 121, 327
- Bovy, J., Rix, H.-W., Green, G. M., Schlafly, E. F., & Finkbeiner, D. P. 2016, *ApJ*, 818, 130
- Brown, T. M., Gilliland, R. L., Noyes, R. W., & Ramsey, L. W. 1991, *ApJ*, 368, 599
- Cabrera-Ziri, I. & Conroy, C. 2022, *MNRAS*, 511, 341
- Catelan, M. 2009, *Ap&SS*, 320, 261
- Chen, X., Zhang, J., Wang, S., & Deng, L. 2023, *Nature Astronomy*, 7, 1081
- Choi, J., Dotter, A., Conroy, C., et al. 2016, *ApJ*, 823, 102
- Chontos, A., Huber, D., Sayeed, M., & Yamsiri, P. 2022, *The Journal of Open Source Software*, 7, 3331
- Creevey, O. L., Sordo, R., Pailier, F., et al. 2023, *A&A*, 674, A26
- Cruz Reyes, M., Anderson, R. I., Johansson, L., Netzel, H., & Medaric, Z. 2024, *A&A*, 684, A173
- Di Criscienzo, M., Marconi, M., & Caputo, F. 2004, *ApJ*, 612, 1092
- Dziembowski, W. 1977, *Acta Astron.*, 27, 95
- Dziembowski, W. A. 2016, *Communications of the Konkoly Observatory Hungary*, 105, 23
- Gaia Collaboration, Brown, A. G. A., Vallenari, A., et al. 2021, *A&A*, 649, A1
- Gratton, R. G., Carretta, E., Bragaglia, A., Lucatello, S., & D’Orazi, V. 2010, *A&A*, 517, A81
- Green, G. M., Schlafly, E., Zucker, C., Speagle, J. S., & Finkbeiner, D. 2019, *ApJ*, 887, 93
- Hajdu, G., Catelan, M., Jurcsik, J., et al. 2015, *MNRAS*, 449, L113
- Hajdu, G., Pietrzyński, G., Jurcsik, J., et al. 2021, *ApJ*, 915, 50
- Harris, W. E. 1996, *AJ*, 112, 1487
- Hendricks, B., Stetson, P. B., VandenBerg, D. A., & Dall’Ora, M. 2012, *AJ*, 144, 25
- Hinkel, N. R., Young, P. A., & Wheeler, Caleb H., I. 2022, *AJ*, 164, 256
- Howell, M., Campbell, S. W., Stello, D., & De Silva, G. M. 2022, *MNRAS*, 515, 3184
- Howell, M., Campbell, S. W., Stello, D., & De Silva, G. M. 2024, *MNRAS*, 527, 7974
- Joyce, M., Johnson, C. I., Marchetti, T., et al. 2023, *ApJ*, 946, 28
- Joyce, M., Molnár, L., Cinquegrana, G., et al. 2024, *ApJ*, 971, 186
- Joyce, M. & Tayar, J. 2023, *Galaxies*, 11, 75
- Jurcsik, J. 1998, *A&A*, 333, 571
- Kalup, C. E., Molnár, L., Kiss, C., et al. 2021, *ApJS*, 254, 7
- Karczmarek, P., Wiktorowicz, G., Iłkiewicz, K., et al. 2017, *MNRAS*, 466, 2842
- Kennedy, C. R., Stancliffe, R. J., Kuehn, C., et al. 2014, *ApJ*, 787, 6
- Kjeldsen, H. & Bedding, T. R. 1995, *A&A*, 293, 87
- Kovács, G. B., Nuspl, J., & Szabó, R. 2023, *MNRAS*, 521, 4878
- Kumar, N., Bhardwaj, A., Singh, H. P., et al. 2024, *MNRAS*, 531, 2976
- Kurtz, D. W. 2022, *ARA&A*, 60, 31
- Lenz, P. & Breger, M. 2005, *Communications in Asteroseismology*, 146, 53
- MacLean, B. T., Campbell, S. W., Amarsi, A. M., et al. 2018, *MNRAS*, 481, 373
- Marconi, M., Bono, G., Pietrinferni, A., et al. 2018, *ApJ*, 864, L13
- Marconi, M., Caputo, F., Di Criscienzo, M., & Castellani, M. 2003, *ApJ*, 596, 299
- Marconi, M., Coppola, G., Bono, G., et al. 2015, *ApJ*, 808, 50
- Marino, A. F., Villanova, S., Piotto, G., et al. 2008, *A&A*, 490, 625
- Matteuzzi, M., Montalbán, J., Miglio, A., et al. 2023, *A&A*, 671, A53
- Miglio, A., Girardi, L., Grundahl, F., et al. 2021, *Experimental Astronomy*, 51, 963
- Mochejska, B. J., Kaluzny, J., Thompson, I., & Pych, W. 2002, *AJ*, 124, 1486
- Molnár, L., Kalup, C., & Joyce, M. 2023a, arXiv e-prints, arXiv:2306.12459
- Molnár, L., Pál, A., Plachy, E., et al. 2015a, *ApJ*, 812, 2
- Molnár, L., Pál, A., Sárneczky, K., et al. 2018, *ApJS*, 234, 37
- Molnár, L., Plachy, E., Bódi, A., et al. 2023b, *A&A*, 678, A104
- Molnár, L., Szabó, R., Moskalik, P. A., et al. 2015b, *MNRAS*, 452, 4283
- Momany, Y., Piotto, G., Recio-Blanco, A., et al. 2002, *ApJ*, 576, L65
- Mucciarelli, A. & Bellazzini, M. 2020, *Research Notes of the American Astronomical Society*, 4, 52
- Nemec, J. M., Smolec, R., Benkó, J. M., et al. 2011, *MNRAS*, 417, 1022
- Netzel, H., Molnár, L., & Joyce, M. 2023, *MNRAS*, 525, 5378
- Netzel, H. & Smolec, R. 2019, *MNRAS*, 487, 5584
- Netzel, H. & Smolec, R. 2022, *MNRAS*, 515, 3439
- Netzel, H., Smolec, R., & Dziembowski, W. 2015a, *MNRAS*, 451, L25
- Netzel, H., Smolec, R., & Moskalik, P. 2015b, *MNRAS*, 447, 1173
- Netzel, H., Smolec, R., & Moskalik, P. 2015c, *MNRAS*, 453, 2022
- Netzel, H., Varga, V., Szabo, R., Smolec, R., & Plachy, E. 2024, arXiv e-prints, arXiv:2404.14373
- Pál, A. 2012, *MNRAS*, 421, 1825
- Pietrzyński, G., Thompson, I. B., Gieren, W., et al. 2012, *Nature*, 484, 75
- Plachy, E., Molnár, L., Bódi, A., et al. 2019, *ApJS*, 244, 32
- Reimers, D. 1975, *Memoires of the Societe Royale des Sciences de Liege*, 8, 369
- Riello, M., De Angeli, F., Evans, D. W., et al. 2021, *A&A*, 649, A3
- Safonova, M., Mkrtichian, D., Hasan, P., et al. 2016, *AJ*, 151, 27
- Salaris, M. & Cassisi, S. 2006, *Evolution of Stars and Stellar Populations* (Wiley)
- Salaris, M., Chieffi, A., & Straniero, O. 1993, *ApJ*, 414, 580
- Shapley, H. 1916, *ApJ*, 43, 217
- Smolec, R. & Moskalik, P. 2008, *Acta Astron.*, 58, 193
- Smolec, R., Moskalik, P., Kałużny, J., et al. 2017, *MNRAS*, 467, 2349
- Stello, D., Chaplin, W. J., Basu, S., Elsworth, Y., & Bedding, T. R. 2009, *MNRAS*, 400, L80
- Stetson, P. B., Braga, V. F., Dall’Ora, M., et al. 2014, *PASP*, 126, 521
- Szabó, R., Kolláth, Z., & Buchler, J. R. 2004, *A&A*, 425, 627
- Ulrich, R. K. 1986, *ApJ*, 306, L37
- Valcarce, A. A. R. & Catelan, M. 2008, *A&A*, 487, 185
- van Albada, T. S. & Baker, N. 1971, *ApJ*, 169, 311
- Vasiliev, E. & Baumgardt, H. 2021, *MNRAS*, 505, 5978
- Wade, R. A., Donley, J., Fried, R., White, R. E., & Saha, A. 1999, *AJ*, 118, 2442
- Wallace, J. J., Hartman, J. D., Bakos, G. Á., & Bhatti, W. 2019a, *ApJS*, 244, 12
- Wallace, J. J., Hartman, J. D., Bakos, G. Á., & Bhatti, W. 2019b, *ApJ*, 870, L7
- Yao, B. A., Tong, J. H., & Zhang, C. S. 1988, *Acta Astronomica Sinica*, 29, 243

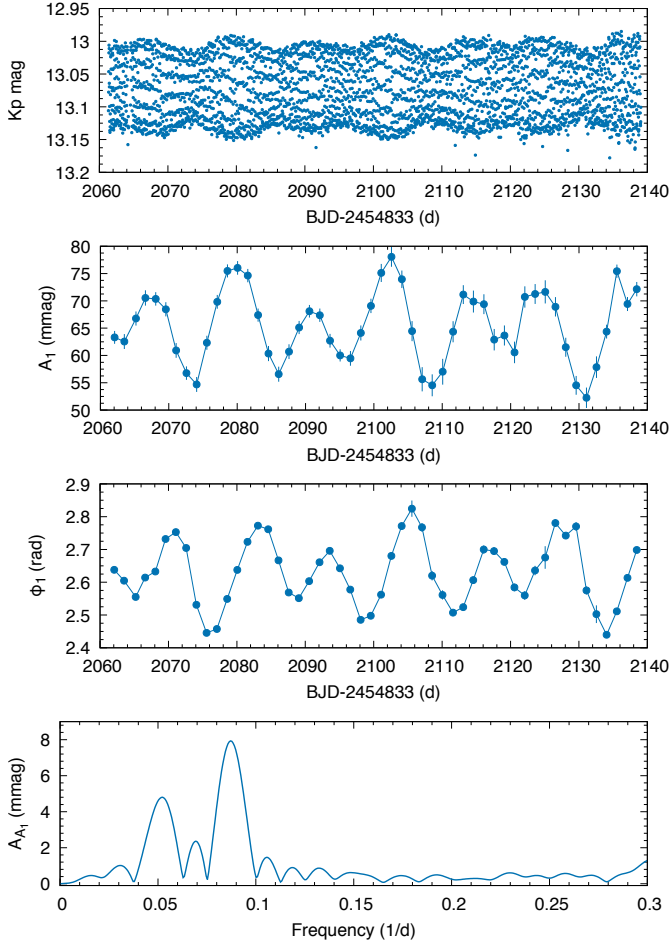


Fig. B.1. V61 amplitude and phase modulation

Appendix A: V61, the modulated star

The light curve of V61 has a much lower pulsation amplitude compared to the others and shows amplitude and phase modulations. This pattern is very similar to the modulated low-amplitude RRc stars observed in M80 Molnár et al. (2023b) and elsewhere (Antipin & Jurcsik 2005; Smolec et al. 2017; Netzel & Smolec 2019). Just like in those cases, we detect asymmetry side peaks next to the pulsation frequency, in this case, above it. We cut the light curve into 1.5 d long segments and fitted A_1 and ϕ_1 for each segment separately with the same, fixed f_1 frequency to study the shape of the modulation more closely.

As Figure B.1 shows, the modulation pattern is multiperiodic. We calculated the Fourier-spectra of both the amplitude and phase variations. The former is also shown in Fig. B.1; the spectrum of the phase variation looks very similar. Both show to separate frequency peak, from which we calculated two modulation periods: $P_{m1} = 11.39 \pm 0.05$ d and $P_{m2} = 19.63 \pm 0.25$ d.

Appendix B: Data tables

In Table B.1, we present the reduced K2 light curves for the five RRc stars analysed in this work. The full table will be available online. In Table B.4, we list the updated seismic and physical parameters for the RGB, AGB and rHB stars. In Tables B.2 and B.3 we list the mass estimates we show in Figures 9 and 10.

Table B.1. K2SC- and trend-corrected photometric data for the five RRc stars. The full table is available in machine-readable format online.

ID	BJD-2454833 (d)	Kp (mag)	ΔK_p (mag)
V06	2060.284202	13.41794	0.00102
V06	2060.304635	13.34582	0.00094
V06	2060.325067	13.22527	0.00084
V06	2060.345499	13.16045	0.00080
V06	2060.365931	13.12550	0.00078
V06	2060.386363	13.09217	0.00076
V06	2060.406796	13.08390	0.00076
V06	2060.427228	13.10122	0.00077
...			

Table B.2. Mass values for RR Lyrae and rHB stars based on the mass relation of Gratton et al. (2010), compared to our seismic masses.

ID	$M_{\text{Gratton2010}}$	M_{seism}
V06	0.633 ± 0.011	0.631 ± 0.016
V42	0.630 ± 0.011	0.647 ± 0.014
V43	0.625 ± 0.011	0.683 ± 0.035
V76	0.635 ± 0.011	0.667 ± 0.026
V61	0.627 ± 0.011	0.751 ± 0.021
M4RHB39	0.671 ± 0.010	0.66 ± 0.05
M4RHB41	0.675 ± 0.011	0.68 ± 0.05
M4RHB42	0.662 ± 0.010	0.63 ± 0.05
M4RHB44	0.664 ± 0.010	0.66 ± 0.05
M4RHB127	0.661 ± 0.010	0.55 ± 0.04
M4RHB196	0.676 ± 0.012	0.66 ± 0.05
M4RHB201	0.666 ± 0.012	0.62 ± 0.05
M4RHB202	0.663 ± 0.012	0.65 ± 0.06

Table B.3. Mass values calculated from the various mass relations, using either the classical observational constraints or the physical parameters from our seismic fits as constraints.

ID	M_{seism}	vA-B1971	B1997	J1998	M2003	dC2004	M2015
classical constraints							
V06	0.631 ± 0.016	0.693 ± 0.051	0.692 ± 0.033	0.715 ± 0.034	0.691 ± 0.033	0.693 ± 0.038	0.763 ± 0.041
V42	0.647 ± 0.014	0.689 ± 0.050	0.690 ± 0.032	0.707 ± 0.034	0.690 ± 0.032	0.691 ± 0.038	0.758 ± 0.041
V43	0.683 ± 0.035	0.585 ± 0.146	0.576 ± 0.096	0.579 ± 0.102	0.578 ± 0.095	0.587 ± 0.099	0.624 ± 0.097
V76	0.667 ± 0.026	0.591 ± 0.186	0.584 ± 0.122	0.583 ± 0.130	0.587 ± 0.121	0.595 ± 0.124	0.632 ± 0.120
V61	0.751 ± 0.021	0.671 ± 0.184	0.679 ± 0.118	0.680 ± 0.126	0.680 ± 0.117	0.679 ± 0.121	0.740 ± 0.114
seismic constraints							
V06	0.631 ± 0.016	0.609 ± 0.013	0.601 ± 0.008	0.610 ± 0.009	0.602 ± 0.008	0.609 ± 0.023	0.654 ± 0.033
V42	0.647 ± 0.014	0.625 ± 0.013	0.621 ± 0.008	0.627 ± 0.009	0.622 ± 0.008	0.627 ± 0.022	0.676 ± 0.032
V43	0.683 ± 0.035	0.657 ± 0.055	0.653 ± 0.036	0.666 ± 0.038	0.655 ± 0.036	0.660 ± 0.042	0.716 ± 0.045
V76	0.667 ± 0.026	0.645 ± 0.055	0.642 ± 0.036	0.648 ± 0.038	0.645 ± 0.036	0.650 ± 0.041	0.701 ± 0.045
V61	0.751 ± 0.021	0.711 ± 0.011	0.723 ± 0.007	0.730 ± 0.007	0.723 ± 0.007	0.720 ± 0.019	0.792 ± 0.027

Table B.4. The updated global seismic properties and calculated physical parameters for the giants in M4.

ID	Type	QF	G (mag)	ν_{max} (μHz)	$\Delta\nu_{\text{max}}$ (μHz)	T_{eff} (K)	ΔT_{eff} (K)	L (L_{\odot})	ΔL_{rand} (L_{\odot})	ΔL_{sys} (L_{\odot})	M (M_{\odot})	ΔM (M_{\odot})
M4AGB01	AGB	MD	12.08	9.60	0.40	4944	29	104.1	0.9	12.1	0.56	0.03
M4AGB02	AGB	D	11.84	6.67	0.13	4838	62	128.3	2.6	14.9	0.51	0.03
M4RGB58	RGB	D	11.97	10.32	0.27	4840	108	122.3	4.1	14.2	0.76	0.06
M4AGB59	AGB	MD	11.36	4.73	0.18	5029	108	209.0	5.5	24.3	0.52	0.04
M4AGB62	AGB	D	11.93	8.08	0.09	4941	52	125.3	1.9	14.6	0.56	0.02
M4RGB10	RGB	D	13.40	48.50	0.47	4960	65	32.3	0.6	3.7	0.86	0.04
M4RGB11	RGB	D	12.22	10.74	0.22	4612	58	92.9	2.4	10.8	0.71	0.04
M4RGB13	RGB	D	13.53	49.20	1.99	4840	108	27.0	0.9	3.1	0.79	0.07
M4RGB14	RGB	D	13.09	33.41	0.19	4807	59	41.2	0.8	4.8	0.84	0.04
M4RGB15	RGB	MD	12.59	17.55	0.76	4865	51	65.2	1.1	7.6	0.67	0.04
M4RGB16	RGB	D	13.30	44.02	0.76	4921	62	30.8	0.6	3.6	0.77	0.04
M4RGB17	RGB	D	13.55	51.89	0.71	4785	61	28.4	0.6	3.3	0.92	0.05
M4RGB20	RGB	MD	12.10	10.86	0.35	4535	59	103.0	3.0	11.9	0.84	0.05
M4RGB21	RGB	MD	12.93	31.62	0.95	4855	59	44.2	0.8	5.1	0.83	0.05
M4RGB22	RGB	D	13.23	36.93	1.42	4852	61	35.4	0.7	4.1	0.78	0.05
M4RGB23	RGB	D	13.38	42.55	1.04	4897	108	31.3	1.0	3.6	0.77	0.06
M4RGB24	RGB	D	13.31	45.05	0.47	4829	108	31.8	1.1	3.7	0.86	0.07
M4RGB25	RGB	D	12.70	19.79	0.57	4719	108	60.1	2.4	7.0	0.78	0.07
M4RGB26	RGB	D	11.65	5.81	0.13	4541	79	158.5	6.1	18.4	0.69	0.05
M4RGB27	RGB	D	13.78	69.85	0.85	4954	108	21.0	0.6	2.4	0.81	0.06
M4RGB28	RGB	MD	14.39	126.69	2.51	5157	108	13.0	0.3	1.5	0.79	0.06
M4RGB29	RGB	D	13.51	58.99	0.57	4986	60	24.7	0.4	2.9	0.79	0.04
M4RGB30	RGB	MD	13.01	30.41	0.95	4913	67	43.1	0.8	5.0	0.75	0.04
M4RGB31	RGB	MD	13.60	57.77	1.14	4966	63	25.9	0.5	3.0	0.82	0.04
M4RGB32	RGB	MD	13.85	74.71	1.04	5026	65	20.4	0.3	2.4	0.80	0.04
M4RGB34	RGB	D	14.28	116.59	2.46	5059	108	13.4	0.3	1.6	0.80	0.06
M4RGB35	RGB	D	13.06	32.07	0.57	4838	77	42.1	1.0	4.9	0.81	0.05
M4RGB36	RGB	D	13.03	34.24	1.42	4808	60	47.7	1.0	5.5	1.00	0.06
M4RGB37	RGB	D	13.15	35.14	0.66	4821	108	39.6	1.4	4.6	0.85	0.07
M4RGB48	RGB	D	12.56	17.88	0.22	4746	57	71.3	1.5	8.3	0.82	0.04
M4RGB104	RGB	D	13.15	33.73	0.57	4851	108	38.9	1.3	4.5	0.78	0.06
M4RGB124	RGB	D	14.05	91.66	1.04	5088	108	17.1	0.4	2.0	0.79	0.06
M4RGB129	RGB	D	13.77	70.17	1.99	4989	108	22.6	0.6	2.6	0.86	0.07
M4RGB130	RGB	D	13.08	36.93	0.57	4897	108	40.2	1.2	4.7	0.85	0.07
M4RGB131	RGB	D	14.07	96.96	1.61	5047	108	16.9	0.4	2.0	0.85	0.07
M4RGB133	RGB	D	11.15	3.23	0.04	4377	108	260.0	17.1	30.1	0.72	0.08
M4RGB142	RGB	D	13.86	74.97	1.56	4988	74	22.5	0.4	2.6	0.91	0.05
M4RGB143	RGB	D	13.64	66.72	1.71	4937	108	23.2	0.7	2.7	0.87	0.07
M4RGB147	RGB	D	14.02	103.68	1.61	5218	108	18.5	0.4	2.1	0.88	0.07
M4RGB148	RGB	D	12.45	12.29	0.53	4632	54	76.4	1.8	8.9	0.66	0.04
M4RGB165	RGB	D	13.99	91.85	2.09	5287	108	23.0	0.4	2.7	0.93	0.07

Table B.4. continued.

ID	Type	Quality	G (mag)	ν_{\max} (μHz)	$\Delta\nu_{\max}$ (μHz)	T_{eff} (K)	ΔT_{eff} (K)	L (L_{\odot})	ΔL_{rand} (L_{\odot})	ΔL_{sys} (L_{\odot})	M (M_{\odot})	ΔM (M_{\odot})
M4RGB169	RGB	D	13.75	80.08	2.04	5143	73	24.8	0.4	2.9	0.96	0.05
M4RGB180	RGB	MD	12.90	23.88	0.57	4972	66	54.0	1.0	6.3	0.70	0.04
M4RGB188	RGB	D	13.05	30.98	0.57	4810	108	44.0	1.5	5.1	0.84	0.07
M4RGB190	RGB	MD	13.67	61.41	1.61	4949	108	23.1	0.7	2.7	0.79	0.06
M4RGB191	RGB	MD	13.37	40.25	0.57	4892	61	32.9	0.6	3.8	0.76	0.04
M4RGB194	RGB	MD	13.98	80.21	1.23	5035	72	18.0	0.3	2.1	0.76	0.04
M4RGB195	RGB	D	12.08	8.65	0.09	4687	59	105.9	2.5	12.3	0.61	0.03
M4RGB197	RGB	D	12.53	17.22	0.18	4734	108	72.7	2.8	8.5	0.81	0.07
M4RGB205	RGB	D	13.70	62.18	0.76	4971	61	24.4	0.4	2.8	0.83	0.04
M4RGB210	RGB	D	14.18	102.33	1.52	5093	46	15.2	0.2	1.8	0.78	0.03
M4RGB213	RGB	D	13.67	53.68	0.85	4836	73	25.6	0.6	3.0	0.83	0.05
M4RGB215	RGB	D	14.19	127.78	2.56	5174	92	15.0	0.6	1.7	0.91	0.07
M4RGB216	RGB	MD	13.04	29.57	0.47	4813	108	46.3	1.6	5.4	0.84	0.07
M4RGB217	RGB	D	13.36	51.25	2.18	5015	60	36.7	0.6	4.3	0.99	0.06
M4RGB225	RGB	D	11.20	3.39	0.04	4427	55	258.5	8.5	30.0	0.72	0.04
M4RGB229	RGB	D	12.51	15.95	0.18	4677	54	73.9	1.6	8.6	0.80	0.04
M4RGB238	RGB	MD	13.91	83.79	1.71	5065	74	20.3	0.4	2.4	0.87	0.05
M4RGB244	RGB	D	13.05	32.13	0.19	4877	62	44.2	0.8	5.1	0.83	0.04
M4RGB252	RGB	D	13.58	55.28	0.66	5012	60	26.7	0.4	3.1	0.78	0.04
M4RGB358	RGB	MD	12.94	27.02	1.14	4814	90	47.1	1.4	5.5	0.78	0.06
M4RGB363	RGB	MD	11.90	7.93	0.22	4633	78	128.8	4.2	15.0	0.71	0.05
M4RGB365	RGB	MD	11.71	6.41	0.14	4540	51	152.9	3.9	17.7	0.73	0.04
M4RGB408	RGB	MD	12.44	13.61	0.66	4672	108	80.8	3.4	9.4	0.75	0.07
M4RHB127	RHB	MD	12.99	36.61	1.33	5712	108	45.1	0.5	5.2	0.55	0.04
M4RHB39	RHB	D	13.00	36.88	1.61	5358	108	42.8	0.7	5.0	0.66	0.05
M4RHB41	RHB	D	13.04	36.42	0.57	5284	108	42.4	0.8	4.9	0.68	0.05
M4RHB42	RHB	D	13.00	41.85	1.75	5545	108	40.7	0.6	4.7	0.63	0.05
M4RHB44	RHB	D	13.03	39.70	1.33	5477	108	42.9	0.7	5.0	0.66	0.05
M4RHB47	RHB	MD	13.01	29.45	1.61	5568	108	47.1	0.6	5.5	0.51	0.04
M4RHB196	RHB	D	13.05	35.71	0.71	5310	108	42.9	0.8	5.0	0.66	0.05
M4RHB201	RHB	MD	12.90	28.74	1.04	5404	108	52.6	0.9	6.1	0.62	0.05
M4RHB202	RHB	MD	13.12	43.32	2.46	5529	108	40.1	0.6	4.7	0.65	0.06
M4RHB246	RHB	MD	13.25	42.94	0.47	5612	108	35.4	0.5	4.1	0.54	0.04
M4RHB261	RHB	D	12.88	42.36	1.61	5915	108	52.9	0.5	6.1	0.67	0.05